Journal of Biomedical Optics

BiomedicalOptics.SPIEDigitalLibrary.org

# Photoacoustic speckle tracking for motion estimation and flow analysis

Hein de Hoop
Heechul Yoon
Kelsey Kubelick
Stanislav Emelianov

SPIE.

Hein de Hoop, Heechul Yoon, Kelsey Kubelick, Stanislav Emelianov, "Photoacoustic speckle tracking for motion estimation and flow analysis," *J. Biomed. Opt.* **23**(9), 096001 (2018), doi: 10.1117/1.JBO.23.9.096001.

# Photoacoustic speckle tracking for motion estimation and flow analysis

**Hein de Hoop,[a,b] Heechul Yoon,[a] Kelsey Kubelick,[c] and Stanislav Emelianov[a,c,*]**
[a]Georgia Institute of Technology, School of Electrical and Computer Engineering, Atlanta, Georgia, United States
[b]Eindhoven University of Technology, Department of Biomedical Engineering, Cardiovascular Biomechanics Group, The Netherlands
[c]Georgia Institute of Technology and Emory University School of Medicine, The Wallace H. Coulter Department of Biomedical Engineering, Atlanta, Georgia, United States

**Abstract.** This study explores photoacoustic (PA) speckle tracking to characterize flow as an alternative to ultrasound (US) speckle tracking or current PA flow imaging methods. In cases where tracking of submicrometer particles is required, the US signal-to-noise ratio and contrast might be low due to limited reflectivity of subwavelength size targets at low concentrations. However, it may be possible to perform more accurate velocimetry using PAs due to different contrast mechanisms utilized in PA imaging. Here, we introduce a PA-based speckle tracking method that overcomes the directional dependence of Doppler imaging and the limited field of view of current correlation-based methods used in PA flow imaging. The feasibility of this method is demonstrated in a potential application—minimally invasive diagnosis of ventricular shunt malfunction, where the velocity of optically absorbing particles was estimated in a shunt catheter using block matching of PA and US signals. Overall, our study demonstrates the potential of the PA-based motion tracking method under various flow rates where US imaging cannot be effectively used for specking tracking because of its low contrast and low signal-to-noise ratio.
 [DOI: 10.1117/1.JBO.23.9.096001]

Keywords: photoacoustic imaging; speckle tracking; motion analysis; flow imaging; shunt malfunction; ultrasound imaging.

Paper 180202R received Apr. 11, 2018; accepted for publication Aug. 20, 2018; published online Sep. 13, 2018.

## 1 Introduction

In the last two decades, the use of photoacoustic (PA) imaging in biomedical applications has been increasing steadily due to its penetration depth, high optical contrast, and high spatial resolution. PA imaging relies on the generation of ultrasound (US) waves by sending short, high-energy nonionizing laser pulses into tissue.[1] Once optically absorbing tissue or particles are irradiated by pulsed laser light, heat deposition, and rapid thermal expansion occur, which, in turn, produce PA waves propagating toward the surface of the tissue. At the surface, these waves are recorded by a US transducer commonly used in diagnostic US. The recorded signals are then used to form an image of depth-resolved optical absorbers at spatial resolutions comparable with those of US imaging. Therefore, using a US probe integrated with optical fibers for light delivery, PA imaging can be performed simultaneously with US imaging—an imaging technology referred as combined US and photoacoustic (USPA) imaging.

Real-time USPA imaging has many advantages, such as being inexpensive, noninvasive, portable, and able to emphasize imaging depth or resolution depending on application. For these reasons, both US and PA imaging are appealing modalities in motion tracking and flow imaging compared with other imaging modalities, such as magnetic resonance imaging (MRI). In theory, the same measurement techniques for displacement tracking can be used for US and PA imaging. Compared with US imaging, the promise of PA imaging is that it relies on the absorption of light instead of the backscattering of sound, thus employing a different contrast mechanism. If the duration of the laser pulse is short enough to meet thermal and, in many cases, stress confinement, PA imaging at the desired optical wavelengths should allow tracking of small optically absorbing particles at low concentrations that otherwise may not be detectable by US imaging.[2,3] Several methods for PA flow imaging have been developed, but these methods have drawbacks that currently prevent their use in clinical or preclinical applications.[2]

PA Doppler velocimetry is capable of tracking the movement of light-absorbing particles using intensity-modulated laser light to create a Doppler-shifted PA response. However, similar to Doppler US, the directional dependence of the Doppler shift is a limitation in imaging curved vessels, especially if the exact orientation of the vessel is unknown.[4] Cross-correlation-based methods overcome this limitation by interrogating slow-time PA profiles at two scan lines and estimating the time shift over that distance. A downside of this method is that the accuracy depends on the distance between the two interrogated beams. With a greater distance between the beams, particles could move out of the laser illumination plane, yet with a shorter distance there is a possibility that particles are only detected at one of the two laser beams. Moreover, this method is one-dimensional (1-D), providing only a velocity estimation between two selected locations in the lateral dimension of the imaging plane.[5]

In addition to PA Doppler velocimetry, other PA flow measurement techniques were developed. For example, flow can be evaluated by measuring the transit time of particles in the focal plane of the pulsed laser. However, no directional information of flow is obtained and the maximum measurable velocity is limited by the laser focal spot size and the laser pulse repetition frequency.[6,7] Other PA flow imaging techniques rely on the laser-induced shape transition of nanoparticles resulting in

*Address all correspondence to: Stanislav Emelianov, E-mail: stas@gatech.edu

1083-3668/2018/$25.00 © 2018 SPIE

a difference in PA amplitude. The rate of amplitude change is proportional to the flow speed of the contrast agents and allows for a 1-D estimation of velocity if the fluence of the laser remains constant.[8,9] A PA flowgraphy method is able to estimate blood flow two-dimensionally (2-D) by tracking the PA signal of the wavefront of a confined volume of blood that is heated up by focused US. Detecting the thermal propagation of fluid allows for the estimation of the flow velocity and profile of the wavefront, but the method is not able to track frame-to-frame displacements at every position within the field of view of the vessel.[10]

To avoid these limitations, a motion tracking approach based on block matching of 2-D PA radiofrequency (RF) signals can be used. This approach is already commonly used in US imaging in the form of speckle tracking to quantify motion and deformation of tissue.[3] However, in certain applications the signal-to-noise ratio (SNR) of the US signal may be too low to perform accurate US velocimetry. In such cases, it may be possible to track the motion of particles or tissue within the region of interest (ROI) using the PA signal because it relies on a different imaging contrast phenomenon. In this paper, we investigate the use of PA speckle tracking to perform motion estimation and flow analysis of either cells or polymer particles labeled with optically absorbing nanoparticles. Due to size difference, the cells and polymer particles have very different acoustic backscattering properties allowing comparison between traditional US velocimetry and our PA speckle tracking method.

As an example, we demonstrate the performance of block matching of PA signals to identify ventricular shunt malfunction based on flow velocity estimation and quantification of flow rate in a shunt catheter. Ventricular shunt catheters are placed in patients affected by hydrocephalus, a condition where intracranial pressure rises due to an increase in cerebrospinal fluid (CSF).[11] The shunt system drains excess CSF, and, in most systems, the rate of drainage can be adjusted by a noninvasive or minimally invasive procedure. Monitoring and regular medical follow up is required to ensure the functionality of these shunt systems because malfunctions, including over-drainage or obstruction, leakage, and breaking of the tube causing under-drainage, appear frequently.[12]

As hydrocephalus is most common with infants and diagnosis of the shunt catheter is performed on a regular basis, a fast, noninvasive method to measure CSF flow in the catheter is required to determine the need for further imaging and intervention. Because CSF primarily consists of water containing low concentrations of cells, proteins, and ions, it does not provide sufficient US backscattered signal.[13] To detect the flow of the CSF fluid, contrast agents are often injected into a valve chamber, and the flow of the contrast agent is monitored to assess shunt functionality, including flow velocity.[14]

In our recent work, using a phantom consisting of a ventricular shunt catheter, we demonstrated the potential for diagnosing shunt malfunctions by performing speckle tracking of microbubbles based on their linear or nonlinear US response.[15,16] However, the method is limited by the angular dependence of US and the large diameter of microbubbles. If the shunt catheter malfunctions due to partial obstruction, microbubbles may block the flow. Furthermore, due to microbubble buoyancy, measurements at slow flow rates may be affected. These aspects may limit clinical utility of microbubble-based US methods to detect shunt catheter malfunction. Therefore, it is desirable to use smaller, submicrometer particles as contrast agents, and nanoparticle-augmented PA imaging may better facilitate minimally invasive CSF flow measurements. To explore this approach, we have investigated the quantification of flow of light-absorbing particles by tracking the US and PA RF signals from the particles in a ventricular shunt catheter. Overall, this study aims to demonstrate the potential and feasibility of performing quantitative flow measurements using a PA block-matching algorithm as an alternative to PA Doppler.

## 2 Materials and Methods

### 2.1 *Contrast Agents*

To demonstrate the potential of PA-based speckle tracking in situations with insufficient US SNR, two contrast agents with different acoustic properties were used. Specifically, we created photoabsorbing contrast agents of two different sizes by loading two different vehicles with optically absorbing nanoparticles. One of the contrast agents was MDA-MB 231 human breast cancer cells incubated with Prussian blue nanocubes (PBNC-cells), simulating applications where the particle of interest produces both US and PA signals. The second contrast agent was polylactic-co-glycolic acid (PLGA) nanoparticles loaded with PBNCs (PBNC–PLGA), simulating applications where the particle of interest is too small for US imaging and is better detected by PA imaging.

PBNCs were synthesized using previously developed protocols.[17] PBNCs with a width of ∼20 nm edge length were produced via a seed-mediated method using 2 nm dextran-coated superparamagnetic iron oxide nanoparticles (SPIONs) as cores. Briefly, 60 mg of SPIONs were added to 150 mL of deionized ultrafiltered (DIUF) water, followed by 7.5 mL of reactant, 5% potassium hexacyanoferrate (II) trihydrate [$K_4Fe(CN)_6$ $3H_2O$, Sigma-Aldrich] in DIUF water. After stirring for 1 min, 2.496 mL of catalyst, 1.85% hydrochloric acid (HCl, Sigma-Aldrich) in DIUF water, was added, and the solution was stirred for at least 1 h. The peak optical absorption of PBNCs, measured using a UV–Vis spectrophotometer (Synergy HT Microplate reader, BioTek Instruments), was around 680 nm wavelength.

To create a larger photoabsorbing contrast agent, MDA-MB 231 human breast cancer cells were labeled with PBNCs. The MDA-MB 231 cells were seeded at 5000 cells/cm$^2$ and grown in DMEM-F12 media, supplemented with 10% FBS and 1% penicillin streptomycin. At ∼80% confluency, cells were incubated with the PBNCs overnight in phenol red-free media to allow nanoparticle uptake. After 24 h, cells were washed with phosphate buffered saline (PBS) at least three times to remove excess particles, passaged to collect cells, and centrifuged at 500 RCF to further size separate labeled cells from free PBNCs. The remaining sample consisted of cells loaded with PBNCs (PBNC-cells). PBNC-cells were fixed in neutral buffered formalin for 15 min and resuspended in PBS at a final concentration of $2.06 \times 10^6$ cells/mL. Given the wavelength-dependent optical scattering of the ∼10 $\mu$m diameter cells labeled with PBNCs, the peak absorbance of the solution red-shifted to about 720 nm wavelength as shown in Fig. 1.

To produce smaller photoabsorbing particles, PLGA, (RG502H, Sigma-Aldrich) particles with a diameter of 0.22 $\mu$m were loaded with PBNCs. PLGA particles were synthesized via a water–oil–water double emulsion protocol described elsewhere.[18–21] However, slight modifications were made to decrease the particle size. Briefly, in the first emulsion,

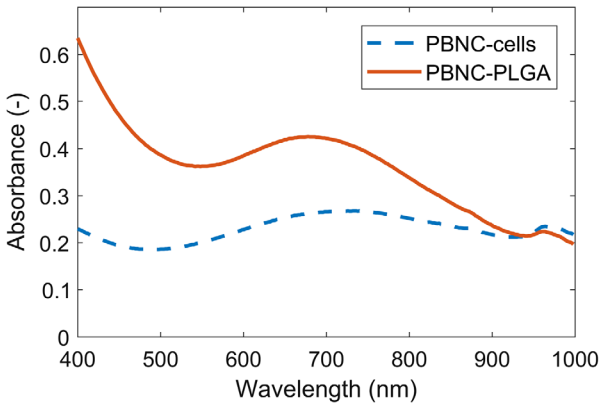


**Fig. 1** Optical absorbance spectrum of MDA-MB 231 cells loaded with PBNC-cells and PLGA particles loaded with PBNCs (PBNC–PLGA) measured by a UV–VIS–NIR spectrophotometer.

PLGA was dissolved in dichloromethane (Sigma-Aldrich) and sonicated at ~85 W in the presence of PBNCs dispersed in DIUF. In the second emulsion, the sample was added to a 5% polyvinyl alcohol (Sigma-Aldrich) solution and sonicated at the same power. After solvent evaporation, the PBNC-PLGA particles were diluted to 8.3 mg/mL to obtain a sufficient volume for the flow experiments. The absorbance spectrum of the PBNC-PLGA particles is shown in Fig. 1. Given the smaller size of the PBNC-PLGA particles and, therefore, less influence of the optical scattering on the absorbance spectrum, the peak of optical absorbance, as expected, was near 690 nm corresponding to the optical absorption of the PBNCs.

### 2.2 *Experimental Setup*

A ventricular shunt catheter from Medtronic, Inc. (Minneapolis, Minnesota) with an inner diameter of 1.2 mm and an outer diameter of 2.4 mm was placed in a water-filled cuvette. The catheter was attached to a 5-mL syringe containing a diluted solution of an optically absorbing contrast agent. The syringe was placed in a syringe pump (Chemyx, Fusion 400) programmed to deliver constant flow rates of 0.01, 0.05, and 0.1 mL/min mimicking low physiological CSF flow rates in a shunt catheter.[22]

The US and PA images of the ventricular catheter were acquired with a Vevo LAZR imaging system (FUJIFILM VisualSonics Inc., Toronto, ON, Canada). The system was equipped with a 40 MHz, 256 element linear array transducer with an integrated fiber optic cable for the delivery of high-energy laser pulses. Laser pulses were transmitted at 20 Hz at wavelengths of 740 and 700 nm for the PBNC-cells and PBNC-PLGA particles, respectively. The transducer was positioned above the catheter tube such that the contrast particles flowed along the lateral direction of the USPA imaging plane. The vertical distance between the transducer and the catheter tube was 11 mm corresponding to the optical focus of the laser beams. Both US and PA images were acquired at a frame rate of 5 Hz. The raw image data were exported to MATLAB (MathWorks, Natick, Massachusetts) for offline analysis and image processing.

### 2.3 *Syringe Pump Calibration*

To confirm whether the programmed flow rate setting on the syringe pump matched the actual flow rate delivered to the shunt catheter, flow calibration experiments were performed for each flow rate setting. Using a 5 mL syringe, DIUF water was injected through the shunt catheter using the same syringe pump described above. The outlet of the catheter was positioned above a vial resting on a microscale (Mettler Toledo, LLC, Columbus, Ohio) such that the output flow could be measured by the change in weight. For each flow rate, the weight displayed on the scale was read every 3 min up to a total of 12 min. The mean of the differential weight values was used to determine the true flow rates in our experimental setup. The average and standard deviation of the true flow rate of each syringe pump flow setting are shown in Table 1.

**Table 1** Syringe pump flow calibration for the flow rates used in the experiments.

| Expected flow rate (mL/min) | Average true flow rate (mL/min) | Standard deviation flow rate (mL/min) |
|---|---|---|
| 0.10 | 0.094 | 0.001 |
| 0.05 | 0.040 | 0.008 |
| 0.01 | 0.009 | 0.001 |

### 2.4 *Data Processing and Block Matching Algorithm*

The US and PA images were exported as in-phase and quadrature (IQ) data from the Vevo LAZR imaging system, and RF data were reconstructed using MATLAB. For every RF line in an image, the IQ data were upsampled by a factor of 8, interpolated by a 63-tap low-pass filter and modulated by the carrier frequency to reconstruct the RF data. The US images covered an area of 14.08 mm × 14 mm, whereas the PA images covered an area of 13.9 mm × 13.88 mm. As a result, the pixel sizes were 0.0552 mm × 0.0016 mm and 0.0544 mm × 0.0034 mm (lateral by axial dimensions) for the US and PA images, respectively. Fifty consecutive imaging frames were used to estimate the average displacements, covering a time span of 10 s.

The pixel displacements between adjacent frames were calculated using a block-matching algorithm based on the sum of squared differences (SSD) as an index for similarity.[23] Figure 2(a) shows a schematic representation of the block-matching algorithm. To estimate the displacement for every pixel within the ROI (e.g., within the lumen of the shunt catheter) of the reference image $f(x, y)$, a 2-D reference kernel containing $k_1 \times k_2$ pixels of RF data was matched for similarity with a target kernel containing $k_1 \times k_2$ pixels of RF data within a search area ($s_1 \times s_2$ pixels) in the target frame $g(x, y)$. The translation of the kernel between frames is represented by the location of the minimum value of the SSD [Fig. 2(b)]:

$$\mathrm{SSD}(s_1, s_2) = \sum_{i=-k_1}^{k_1} \sum_{j=-k_2}^{k_2} [f(x+i, y+j) - g(x+i-s_1, y+j-s_2)]^2. \quad (1)$$

The performance of the block-matching algorithm is influenced by the size of the kernel and the search area. A larger kernel results in spatial averaging of the displacement, thus a smaller kernel is preferred; however, the kernel should contain enough characteristic features of the signal to allow for accurate

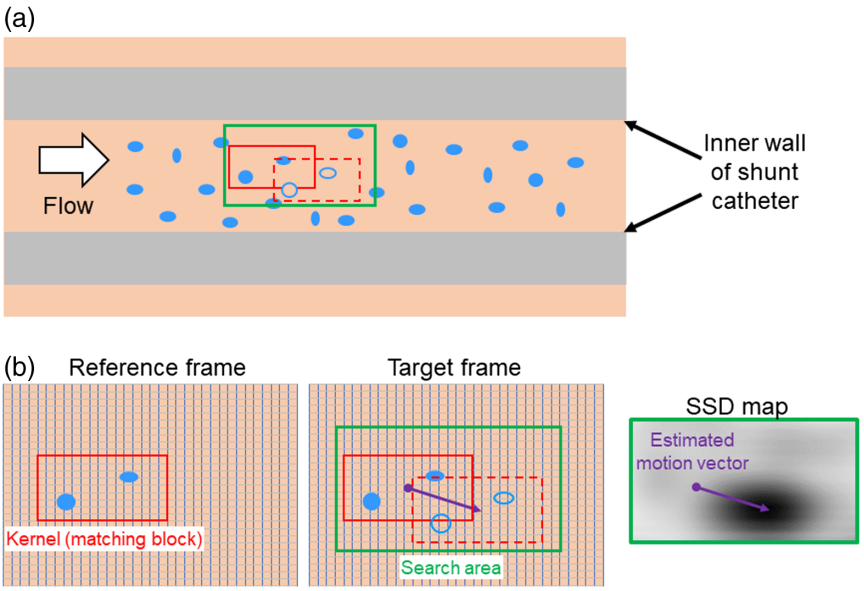


**Fig. 2** Schematic representation of SSD algorithm. (a) The matching block or kernel, and the search area is defined within the shunt catheter where particles are flowing. (b) The SSD map is created by matching the kernel from the reference frame with kernels within the search area—the location of the local minimum in the SSD map indicates the displacement of the kernel between reference and target frames.

displacement estimation. The search area should be large enough to track the displacement at different velocities, but larger search areas increase computational time and increase the likelihood of outliers. For this reason, multiple kernel sizes and shapes were tested and the size of the search area was adapted to the expected flow velocity. A rectangular kernel size of 0.98 mm × 0.11 mm (lateral by axial) was used for both US and PA data. The search area was 0.27 mm in the axial (vertical) direction, varying in lateral direction for slower/faster flows: 1.52 mm for the flow setting of 0.01 mL/min, 1.63 mm for 0.05 mL/min, and 1.74 mm for 0.1 mL/min, respectively.

Without interpolation, the block-matching algorithm outputs the displacements measured in an integer number of pixels, and, therefore, the accuracy of the block-matching algorithm is limited to the pixel size. In our measurements of horizontal flow in the shunt catheter, the lateral dimension of the US and PA pixels was about 0.05 mm. Given constant pixel size, the accuracy of the block-matching algorithm will decrease at lower flow rates where the motion-induced displacements between two adjacent frames can be significantly smaller than one pixel. In addition, even for faster flow rates, the flow is very slow near the catheter wall. Finally, given finite axial extent of the kernel, the measured displacements of contrast particles near the wall will be biased by the stationary signal from the catheter wall where particles were moving slowly. Performing interpolation to reduce the lateral pixel size and to more accurately estimate displacements is a straightforward approach, but it is computationally expensive and will reduce the efficiency of the block-matching algorithm.[24] To overcome this problem, we applied frame decimation for the lowest flow setting of 0.01 mL/min, i.e., the displacements were calculated between interleaved frames. Specifically, the analysis was performed using three-frame increments thereby changing the temporal resolution to 0.6 s between the frames used in the block-matching method. The frame increment size is a trade-off between overcoming subpixel displacements in the regions of slow flow (e.g., near the walls of the shunt catheter) and decorrelation in the regions of faster flow (e.g., center of the shunt catheter).

The displacement estimates between each pair of frames were stored to create a velocity map within the catheter tube. Using the frame rate and the pixel sizes for the US and PA data, the pixel displacements were converted to velocity. The average coordinates of the inner tube walls, identified using the amplitude of the USPA signal, were used to mask the velocity map outside the tube. Within the field of view, the velocity along the width of each lateral line was calculated to estimate the lateral velocity profile between two frames. Assuming the syringe pump provided a constant flow, the velocity profiles were averaged over 50 frames. The acquired velocity profiles were compared with a model of fully developed laminar flow using the true flow rates of the syringe pump used in our experiments. In this model, the lateral flow $v_z$ at each radial position $r$ within the tube is described by the following equation:

$$v_z(r) = 2\frac{q_v}{\pi a^2}\left(1 - \frac{r^2}{a^2}\right), \tag{2}$$

where $a$ is the inner radius of the catheter tube and $q_v$ is the volumetric flow rate.

## 3 Results

US and PA images of the shunt catheter with either PBNC-cells or PBNC-PLGA particles flowing through the shunt catheter are shown in Fig. 3. As indicated by the labels in Fig. 3, the bright horizontal bands in US images represent the inner and outer walls of the ventricular catheter. The lower intensity horizontal bands in the US and PA images are reverberations of sound waves caused by reflections of the inner and outer walls of the catheter tube. We purposely left the reverberations in our images and data to demonstrate the effect of these US/PA imaging artifacts on the velocity measurements. Between the inner

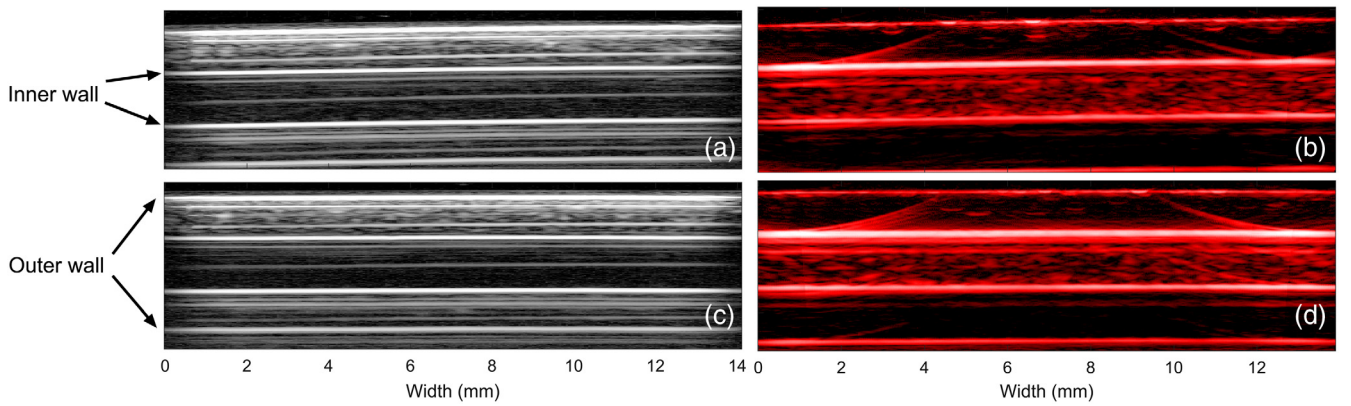


**Fig. 3** Representative (a, c) US and (b, d) PA still images from Video 1 of (a, b) the shunt catheter tube containing PBNC-cells or (c, d) PBNC-PLGA particles under a flow rate of 0.094 mL/min (a scale bar: 1 mm) [Video 1, MP4, 2787.0205 kb (URL: https://doi.org/10.1117/1.JBO.23.9.096001.1)].

walls, the contrast particles are shown—these particles move from left to right (see US and PA cineloops shown in Video 1).

The larger size PBNC-cells provided more backscattered US signals [Fig. 3(a)] compared with the smaller diameter PBNC-PLGA particles [Fig. 3(c)]; however, both PBNC-cells and PBNC-PLGA particles produced a strong PA response that was clearly visible in the PA images [Figs. 3(b) and 3(d)]. In the US and PA cineloops (Video 1), movement of the PBNC-cells and PBNC-PLGA particles can be visually tracked in the PA images, whereas particle tracking was not obvious in the US images and only the movement of the PBNC-cells was depicted.

Figure 4 shows the velocity maps between two adjacent frames for the PA [Fig. 4(a)] and US [Fig. 4(b)] images of PBNC-cells moving at a flow rate of 0.094 mL/min. The upper and lower boundaries of the velocity map were determined by the average coordinates of the inner wall. The lateral extent of the velocity map was reduced due to motion estimation artifacts near the lateral boundaries, where displacement of the particles cannot be reliable estimates. The velocity maps in Fig. 4 are displayed as an overlay on the PA or US images to show the velocity in the user-defined ROI. As shown in the PA data, the estimated amplitude of the velocity was the highest in the middle of the catheter and gradually reduced to zero near the inner walls. The same trend held for the US data; however, the estimated velocity was noisier and/or underestimated in regions where reverberations were present, e.g., in the middle of the shunt catheter [Fig. 4(b)].

To analyze the speckle tracking results of each dataset, the estimated velocity profiles of the PA and US data of the PBNC-cells and PBNC-PLGA particles were compared for each flow rate. The results are shown in Fig. 5, where the average velocity with respect to the radial position of the catheter tube is displayed. The standard deviation of the velocity estimations over 50 frames is shown by the error bars at six positions along the inner diameter of the tube. As a validation, the measurements were compared with the velocity profile obtained from a model of fully developed laminar flow. For the slow flow rate, i.e., true flow rate of 0.0091 mL/min [Figs. 5(e) and 5(f)], the measured velocity profiles were not compared with the model-based velocity profile because the assumption of the laminar flow was not valid at this slow velocity.

As shown in Fig. 5, flow profiles estimated using the PA images of both PBNC-PLGA particles and PBNC-cells were fairly symmetric, indicating expected laminar flow. The small decrease in the velocity amplitude at −0.2 mm away from

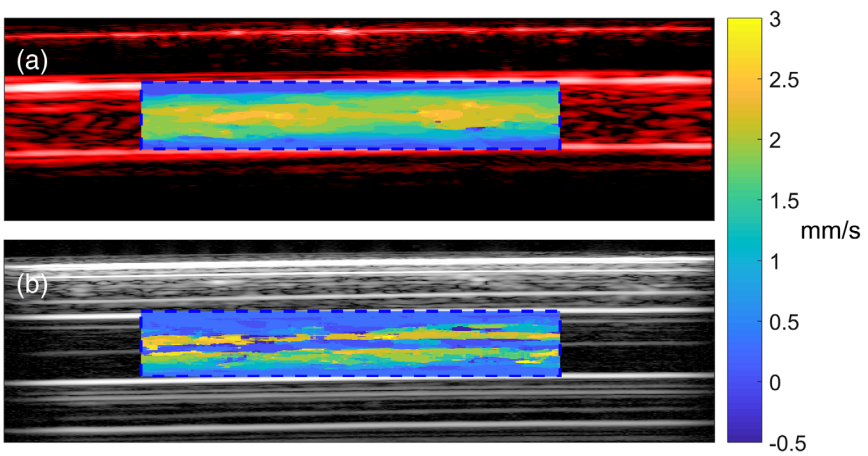


**Fig. 4** Velocity maps of PBNC-cells at a flow rate of 0.094 mL/min estimated between two adjacent (a) PA and (b) US frames.

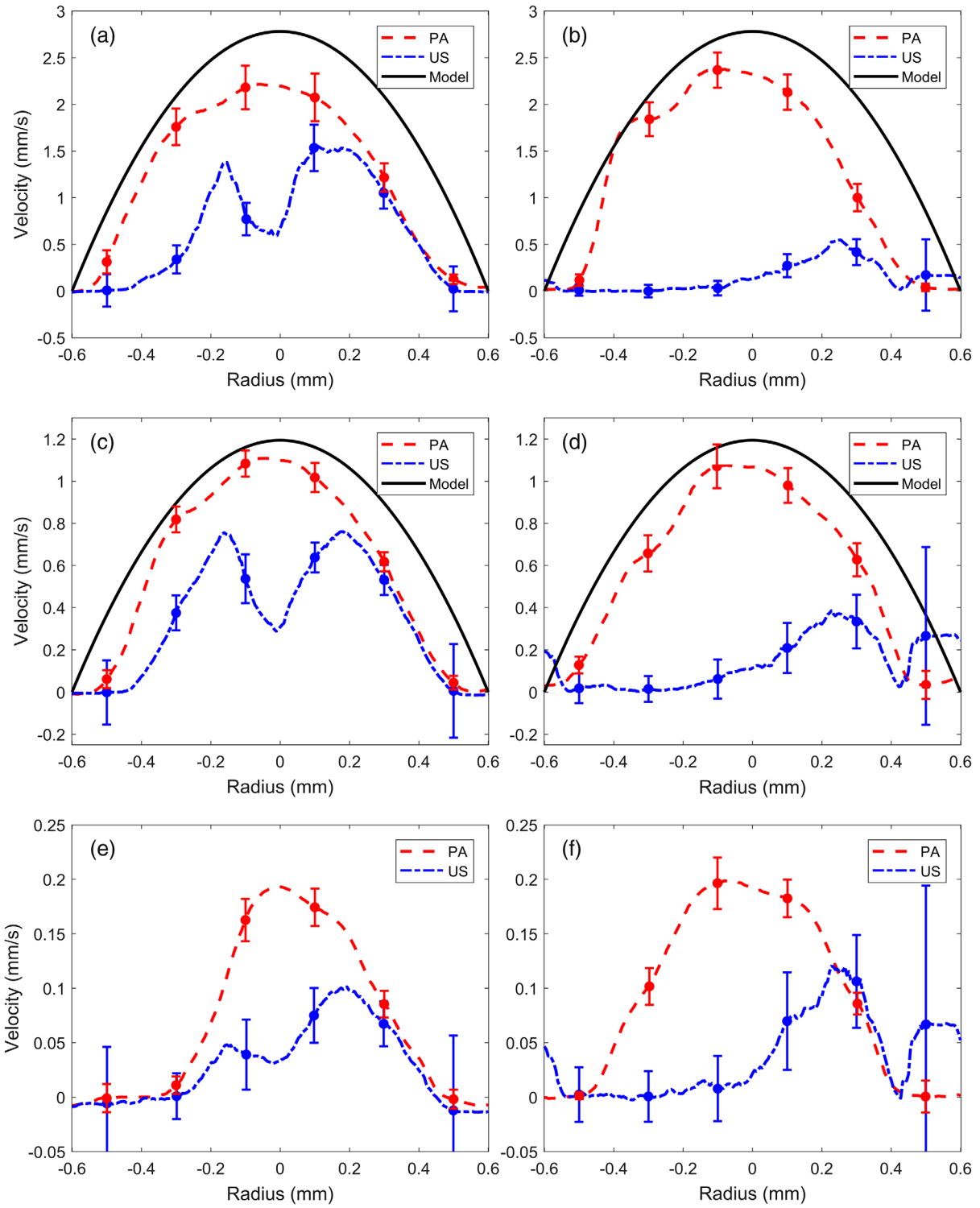


**Fig. 5** Velocity profiles estimated using the PA and US images for (a,c,e) PBNC-cells and (b,d,f) PBNC-PLGA particles at a flow rate of (a,b) 0.094 mL/min, (c,d) 0.040 mL/min, and (e,f) 0.0091 mL/min. Error bars depict the standard deviation of the estimated velocities over 50 frames at the respective radial positions within the tube.

the center [Figs. 5(a)–5(d)] was due to the PA reverberation artifact [Fig. 3(b)], which appeared stationary and, therefore, slightly decreased the measured velocity at that position. The standard deviations were small, ranging from 5% to 10% of the maximum estimated velocity. Compared with the expected flow profiles, there was an overall underestimation for maximum velocities of 2.21 and 2.38 mm/s of the PBNC-cells and PBNC-PLGA particles at a flow rate of 0.094 mL/min, respectively, and 1.11 and 1.08 mm/s compared with an expected 1.19 mm/s for a flow rate of 0.04 mL/min. At a low flow rate of 0.0091 mL/min, the estimated flow profiles are also symmetric but movement close to the edges is more

restricted, likely indicating adhesion of contrast agents to the inner wall of the shunt catheter.

Although the velocity estimations from PA images were generally the same for the PBNC-cells and PBNC-PLGA particles, the estimated velocity profiles using US images were different for the two contrast agents (Fig. 5). The US-based estimates of the flow velocities of the PBNC-cells were overall similar for different flow rates. Due to US reverberation, the velocity profiles show a valley in the center of the catheter [e.g., Fig. 5(a) or Fig. 5(c)], where a reverberation artifact from the inner wall of the tube was present [Fig. 3(a)]. Therefore, the maximum velocities were found not in the center of the catheter but at a radial position of ∼0.2 mm away from the center of the tube. The displacement estimations of the PBNC-PLGA particles resulted in an uneven velocity profile with the highest flow velocity ranging from 0.1 to 0.5 mm/s observed 0.3 mm away from the center of the tube. Clearly, the velocity profile was far from an expected laminar flow. This can be explained by the low signal-to-noise ratio in underlying US images obtained from a low concentration solution of nanometer-scale particles. Overall, there was a large variance in velocity at the edges of the catheter, especially at the radial position of 0.5 mm where the search area included the inner wall of the catheter tube. The standard deviations increased for decreasing flow rates (e.g., standard deviation was largest for a flow of 0.0091 mL/min), which can be related to the decorrelation of image characteristics between frame-pairs as frame decimation was applied to compensate for sub-pixel displacements.

## 4 Discussion and Conclusions

In this study, we performed velocity imaging in a shunt catheter with two PA contrast agents using a block-matching algorithm to estimate fluid motion. We have demonstrated the feasibility of motion tracking using PA signals to estimate the frame-to-frame velocity and compared the performance of the PA block-matching algorithm with US-based tracking. Overall, displacements for larger 10 $\mu$m diameter particles can be detected by tracking the US or PA signal. For smaller, sub-micrometer particles, detecting displacements by tracking the US signal was challenging, whereas PA tracking of the particles was still possible. In other words, for small particles at relatively low concentration, the PA displacement/velocity estimation method described here performed better than US motion tracking over a wide range of flow rates. Therefore, in applications where concentration of small particles is low or reduced concentration is required for safety reasons, PA tracking may perform better if the particles provide sufficient PA signal. For high concentrations of particles, both methods are likely to perform well.

The PBNC-cells and PBNC-PLGA particles were optimized to obtain high SNR in PA images. A peak absorption around 700 nm was a good trade-off between light penetration depth and light absorption of the walls of the catheter, which increased at higher optical wavelengths. The concentration of the contrast agents was comparable between PBNC-cells and PBNC–PLGA particles to create a strong PA response. In US imaging, as a result of the difference in size, the larger PBNC-cells produced stronger US backscattered signal than the PBNC–PLGA particles, being ∼40 times smaller in diameter than the PBNC-cells. This was best observed in the US cineloop (Video 1) or US image (Fig. 3), where the US SNR within the tube was low for PBNC-PLGA particle flow experiments.

For both contrast agents, the block-matching algorithm was able to estimate displacements using the PA RF signals. For flow rates of 0.094 and 0.04 mL/min, velocity profiles with a parabolic flow profile and maximum velocities close to the peak velocity of fully developed laminar flow were estimated. For a flow rate of 0.0091 mL/min, a parabolic velocity profile was still estimated but the velocity of particles near the wall declined rapidly, especially in the case of the PBNC-cells, where the possibility of adhesion of contrast particles to the inner wall was more likely due to their large size.

Displacements of the smaller size low-backscattering PBNC–PLGA particles were more difficult to track using US than the larger PBNC-cells. At each flow rate, the US velocity profiles of the PBNC–PLGA particles were significantly underestimated (Fig. 5). Some movement was detected in the lower half of the tube but at lower precision as the matching kernel contained part of the high-amplitude signal of the inner wall of the catheter tube. Displacements of US speckle were measured for the PBNC-cells but at lower accuracy due to reverberations—imaging artifacts in the US signal. When the kernel contained a static US signal from reverberations and a dynamically changing US signal due to the moving contrast particles, it resulted in an underestimation of the velocity by the block-matching algorithm. This effect was shown in Figs. 4(b) and 5, where there was a drop in estimated lateral velocity in the middle of the tube—the drop was most pronounced in the case of tracking PBNC-cells using US. Similar artifacts were shown in the PA image [Fig. 4(a)] and flow profiles (Fig. 5) although the effect on the velocity estimation was smaller.

The experiments show that in situations where the SNR of the US signal is too low to perform accurate tracking, it is possible to track flow using the PA signal and block-matching techniques. PA imaging relies on a different contrast mechanism and can be performed simultaneously with US imaging.[1] The benefit of using the PA signal for 2-D block matching is that there is no angle dependency as is the case with PA Doppler.[4] Furthermore, regional obstructions or tapering of the vessel could also be identified by displaying the velocity map between frames within the entire area of the vessel within the field of view, which cannot be performed with amplitude encoding techniques.[2,10] This can be useful in diagnosing ventricular shunt malfunction as anomalies in the velocity map may indicate an obstruction or leakage of the shunt catheter. Moreover, the ability to track light-absorbing particles is beneficial because the use of US contrast-enhancing microbubbles should be kept to a minimum dose to prevent unwanted interaction with tissue.[25] These concerns, however, also dictate several strict design criteria for the PA contrast agent.

A limitation of tracking displacement of PA speckle using block-matching algorithms is that the signal from the stationary objects, such as the shunt catheter wall, and imaging artifacts, such as reverberation, affects the velocity estimation in the ROI. To minimize this effect, a rectangular-shaped kernel of 0.98 mm × 0.11 mm (lateral by axial) was used for block matching in the US and PA images. However, the ideal kernel size remains a trade-off between accuracy and precision, as a larger kernel size contains more PA signatures for comparison but also averages the velocity estimation within the kernel and introduces more artifacts from stationary objects. As an example, the signal from the walls in both the US and PA images caused underestimates of the velocity profile of particles moving

near the stationary walls. Furthermore, the current shunt catheter was nontransparent, which led to a large absorption of light at the tube wall and thus a strong PA effect. A transparent catheter tube would reduce the intensity of the PA signal from the wall, thereby decreasing reverberations artifacts within the tube and improving the velocity estimation.

In the future, improvements in the PA motion tracking using block-matching algorithms could be investigated. PA RF-based speckle tracking can be performed in 2-D, which can be useful for the flow estimation in curved vessels or if the flow profile is unknown. More experimental verification could include the use of vector velocity imaging for a direct comparison with the velocity fields measured with PA imaging.

In conclusion, we demonstrated the feasibility of performing motion estimation and flow analysis in a ventricular shunt catheter based on speckle tracking using both PA and US imaging. Although the method was influenced by underestimations near the wall and reverberations, it was able to differentiate the velocities between different clinically relevant flow rates showing the feasibility of PA-based speckle tracking. In the case where contrast particles were too small to be tracked with US, the PA motion tracking method could be an alternative solution to estimate velocities from the PA signals. The ability to track motion in situations where US imaging lacks contrast will be useful in many clinical applications that require or could benefit from assessment using minimally invasive imaging tools.

## Disclosures

No conflicts of interest, financial or otherwise, are declared by the authors.

## Acknowledgments

The authors would like to thank Dr. Jardin Leleux and Dr. Krishnendu Roy at the Georgia Institute of Technology for their help with synthesis of the PLGA particles, and Dr. Lopata for useful discussion of the paper. H.H. would like to thank his parents for making his internship in the Ultrasound Imaging and Therapeutics Research Laboratory at Georgia Tech possible. This work was supported in part by the National Institute of Health under Grant Nos. CA158598 and NS090336.

## References

1. M. H. Xu and L. H. V. Wang, "Photoacoustic imaging in biomedicine," *Rev. Sci. Instrum.* **77**(4), 041101 (2006).
2. P. J. van den Berg, K. Daoudi, and W. Steenbergen, "Review of photoacoustic flow imaging: its current state and its promises," *Photoacoustics* **3**(3), 89–99 (2015).
3. C. Poelma, "Ultrasound imaging velocimetry: a review," *Exp. Fluids* **58**, 3 (2017).
4. H. Fang, K. Maslov, and L. H. V. Wang, "Photoacoustic doppler effect from flowing small light-absorbing particles," *Phys. Rev. Lett.* **99**(18), 18450 (2007).
5. J. Y. Liang et al., "Cross-correlation-based transverse flow measurements using optical resolution photoacoustic microscopy with a digital micromirror device," *J. Biomed. Opt.* **18**(9), 096004 (2013).
6. H. Fang and L. H. V. Wang, "M-mode photoacoustic particle flow imaging," *Opt. Lett.* **34**(5), 671–673 (2009).
7. S. L. Chen et al., "Photoacoustic correlation spectroscopy and its application to low-speed flow measurement," *Opt. Lett.* **35**(8), 1200–1202 (2010).
8. P. C. Li et al., "Photoacoustic flow measurements by use of laser-induced shape transitions of gold nanorods," *Opt. Lett.* **30**(24), 3341–3343 (2005).
9. C. W. Wei et al., "Photoacoustic flow measurements based on wash-in analysis of gold nanorods," *IEEE Trans. Ultrason. Ferroelectr. Freq. Control* **54**(6), 1131–1141 (2007).
10. L. Wang et al., "Ultrasonically encoded photoacoustic flowgraphy in biological tissue," *Phys. Rev. Lett.* **111**(20), 204301 (2013).
11. H. M. Tully and W. B. Dobyns, "Infantile hydrocephalus: a review of epidemiology, classification and causes," *Eur. J. Med. Genet.* **57**(8), 359–368 (2014).
12. C. D. Goeser, M. S. McLeary, and L. W. Young, "Diagnostic imaging of ventriculoperitoneal shunt malfunctions and complications," *Radiographics* **18**(3), 635–651 (1998).
13. B. R. Ransom, "The neuronal microenvironment," in *Medical Physiology: A Cellular and Molecular Approach*, 2nd ed., pp. 289–309, Saunders Elsevier, Philadelphia (2012).
14. V. V. Maller, A. Agarwal, and S. Kanekar, "Imaging of ventricular shunts," *Semin. Ultrasound CT MRI.* **37**(2), 159–173 (2016).
15. R. Hartman et al., "Quantitative contrast-enhanced ultrasound measurement of cerebrospinal fluid flow for the diagnosis of ventricular shunt malfunction," *J. Neurosurg.* **123**(6), 1420–1426 (2015).
16. S. Park et al., "Fluid flow measurement for diagnosis of ventricular shunt malfunction using nonlinear responses of microbubbles in the contrast-enhanced ultrasound imaging," *Jpn. J. Appl. Phys.* **56**, 07JF10 (2017).
17. J. R. Cook et al., "Prussian blue nanocubes: multi-functional nanoparticles for multimodal imaging and image-guided therapy (Conference Presentation)," *Proc. SPIE* **10064**, 100641T (2017).
18. S. P. Kasturi, K. Sachaphibulkij, and K. Roy, "Covalent conjugation of polyethyleneimine on biodegradable microparticles for delivery of plasmid DNA vaccines," *Biomaterials* **26**(32), 6375–6385 (2005).
19. S. P. Kasturi et al., "Prophylactic anti-tumor effects in a B cell lymphoma model with DNA vaccines delivered on polyethylenimine (PEI) functionalized PLGA microparticles," *J. Control. Release* **113**(3), 261–270 (2006).
20. P. Pradhan et al., "The effect of combined IL10 siRNA and CpG ODN as pathogen-mimicking microparticles on Th1/Th2 cytokine balance in dendritic cells and protective immunity against B cell lymphoma," *Biomaterials* **35**(21), 5491–5504 (2014).
21. J. A. Leleux, P. Pradhan, and K. Roy, "Biophysical attributes of CpG presentation control TLR9 signaling to differentially polarize systemic immune responses," *Cell Rep.* **18**(3), 700–710 (2017).
22. C. Kadowaki et al., "Factors affecting cerebrospinal fluid flow in a shunt," *Br. J. Neurosurg.* **1**(4), 467–475 (1987).
23. S. Langeland et al., "Comparison of time-domain displacement estimators for two-dimensional RF tracking," *Ultrasound Med. Biol.* **29**(8), 1177–1186 (2003).
24. E. Konofagou and J. Ophir, "A new elastographic method for estimation and imaging of lateral displacements, lateral strains, corrected axial strains and Poisson's ratios in tissues," *Ultrasound Med. Biol.* **24**(8), 1183–1199 (1998).
25. D. Dalecki, "Biological effects of microbubble-based ultrasound contrast agents," in *Contrast Media in Ultrasonography: Basic Principles and Clinical Applications*, pp. 77–85, Springer-Verlag, Berlin, Heidelberg (2005).

**Hein de Hoop** received his BSc degree in biomedical engineering from the Eindhoven University of Technology in 2016. Currently, he is pursuing his MSc degree in medical engineering within the Photoacoustics and Ultrasound Laboratory Eindhoven. His current research focuses on ultrafast multiperspective ultrasound imaging of the abdominal aorta.

**Heechul Yoon** received his BS and MS degrees in electrical engineering from the Sogang University in 2008 and 2010, respectively. From 2010 to 2014, he worked at Samsung Electronics as a researcher on ultrasound signal/image processing. Currently, he is pursuing PhD studies in electrical and computer engineering at Georgia Institute of Technology. His research interests include development and clinical translation of medical imaging technologies including shear wave elasticity imaging and ultrasound-guided photoacoustic imaging.

**Kelsey Kubelick** received her AB in biological sciences from the University of Chicago in 2012 and her MEng. in biomedical engineering from Duke University with a concentration in tissue engineering in 2013. Currently, she is pursuing her PhD in biomedical engineering at the Georgia Institute of Technology and Emory University. Her research focuses on development of tracking platforms using ultrasound and photoacoustic imaging to expedite translation of novel therapies, particularly in regenerative medicine and immunology.

**Stanislav Emelianov** is a professor of electrical and computer engineering, biomedical engineering, and radiology at the Georgia Institute of Technology and Emory University School of Medicine. Furthermore, he is the director of the Ultrasound Imaging and Therapeutics Research Laboratory. Throughout his career, he has been devoted to the development of advanced imaging methods capable of detecting and diagnosing cancer and other pathologies, assisting treatment planning, and enhancing image-guided therapy and monitoring of the treatment outcome.